April 15, 2003

Infrared aerosol radiative forcing at the surface and the top of the atmosphere

Authors:
K. M. Markowicz, P. J. Flatau, A. M.Vogelmann, P. K. Quinn, and E. J. Welton*

Submission to: Quarterly Journal of the Royal Meteorological Society

We study the aerosol radiative forcing at infrared wavelengths using data from the Aerosol Characterization Experiment (ACE-Asia) cruise of the NOAA R/V Ronald H. Brown. An optical model is derived from chemical measurements, lidar profiles, and visible extinction measurements which is used to and estimate the infrared aerosol optical thickness and the single scattering albedo. The IR model results are compared to detailed Fourier Transform Interferometer based infrared aerosol forcing estimates, pyrgeometer based infrared downward fluxes, and against the direct solar forcing observations. This combined approach attests for the self-consistency of the optical model and allows to derive quantities such as the infrared forcing at the top of the atmosphere or the infrared optical thickness. The mean infrared aerosol optical thickness at 10 μm is 0.08 and the single scattering albedo is 0.55. The modeled infrared aerosol forcing reaches 10 Wm^{-2} during the cruise, which is a significant contribution to the total direct aerosol forcing. The surface infrared aerosol radiative forcing is between 10 to 25% of the shortwave aerosol forcing. The infrared aerosol forcing at the top of the atmosphere can go up to 19% of the solar aerosol forcing. We show good agreement between satellite (CERES instrument) retrievals and model results at the top of the atmosphere. Over the Sea of Japan, the average infrared radiative forcing is 4.6 Wm^{-2} in the window region at the surface and it is 1.5 Wm^{-2} at top of the atmosphere. The top of the atmosphere IR forcing efficiency is a strong function of aerosol temperature and changes between 10 to 18 Wm^{-2} (per infrared optical depth unit), while the surface IR forcing efficiency varies between 37 and 55 Wm^{-2} (per infrared optical depth unit).

* Co-Author: Dr. E. J. Welton
NASA GSFC Code 912
Ellsworth.J.Welton@nasa.gov

Q.J.R.Meteorol. Soc. (2003)

Clear-sky infrared aerosol radiative forcing at the surface and the top of the atmosphere.

By Krzysztof M. Markowicz[1], Piotr J. Flatau[2,3], Andrew M.Vogelmann[3] Patricia K. Quinn[4,5], Ellsworth J. Welton[6]

[1]*Institute of Geophysics, University of Warsaw, Poland*
[2] *UCAR Visiting Scientist at Naval Research Laboratory, Monterey, California*
[3]*Scripps Institution of Oceanography, University of California, San Diego, USA*
[4]*Pacific Marine Environmental Laboratory, NOAA Seattle, Washington*
[5]*Joint Institute for the Study of the Atmosphere and Ocean, University of Washington*
[6]*NASA Goddard Space Flight Center, Code 912, Greenbelt, MD, 20771, USA.*

SUMMARY

We study the clear-sky aerosol radiative forcing at infrared wavelengths using data from the Aerosol Characterization Experiment (ACE-Asia) cruise of the NOAA R/V Ronald H. Brown. Limited number of data points is analyzed mostly from ship and collocated satellite values. An optical model is derived from chemical measurements, lidar profiles, and visible extinction measurements which is used to and estimate the infrared aerosol optical thickness and the single scattering albedo. The IR model results are compared to detailed Fourier Transform Interferometer based infrared aerosol forcing estimates, pyrgeometer based infrared downward fluxes, and against the direct solar forcing observations. This combined approach attests for the self-consistency of the optical model and allows to derive quantities such as the infrared forcing at the top of the atmosphere or the infrared optical thickness. The mean infrared aerosol optical thickness at 10 μm is 0.08 and the single scattering albedo is 0.55. The modeled infrared aerosol forcing reaches 10 Wm^{-2} during the cruise, which is a significant contribution to the total direct aerosol forcing. The surface infrared aerosol radiative forcing is between 10 to 25% of the shortwave aerosol forcing. The infrared aerosol forcing at the top of the atmosphere can go up to 19% of the solar aerosol forcing. We show good agreement between satellite (CERES instrument) retrievals and model results at the top of the atmosphere. Over the Sea of Japan, the average infrared radiative forcing is 4.6 Wm^{-2} in the window region at the surface and it is 1.5 Wm^{-2} at top of the atmosphere. The top of the atmosphere IR forcing efficiency is a strong function of aerosol temperature and changes between 10 to 18 Wm^{-2} (per infrared optical depth unit), while the surface IR forcing efficiency varies between 37 and 55 Wm^{-2} (per infrared optical depth unit).

KEYWORDS: Climate change

1. Introduction

The effects of sea-salt, mineral dust, black carbon, and sulfates in complex environmental conditions are large sources of uncertainty in quantifying regional climate changes

(Houghton, 2001). Much recent work has been devoted to reducing these uncertainties by mounting major observational campaigns: [SCAR-B (Kaufman et al., 1998), TARFOX (Hobbs, 1999), ACE1 (Bates et al., 1998), ACE2 (Raes et al., 2000), INDOEX (Ramanathan et al., 2001), and MINOS (Lelieveld et al., 2002)]. During the Saharan Dust Experiment (SHADE) in Sal, Cape Verde Islands the Airborne Research Interferometer Evaluation System (ARIES) measured 8-12 micron signal of a large Saharan dust storm (*Highwood et al.*, 2002). Their study clearly shows the direct radiative effect of dust in the atmospheric window. Thanks to these complementary activities progress has been reported, but they have been limited mostly to short-wave radiance effect. Direct observations of the infrared (IR) aerosol radiative forcing are rare. The IR radiative effect of aerosol involves many uncertainties and is usually neglected. However new direct observational results (Vogelmann et al., 2003) show that the IR radiative forcing can be significant for natural as well as for anthropogenic aerosol with values that exceed 9 Wm^{-2} (instantaneous value). Other modeling studies indicate that the mineral aerosols have highly varied optical properties that can affect the surface IR flux between 7 and 25 Wm^{-2} (Sokolik et al., 1998). Also, global modeling radiative forcing studies showed large uncertainties due to mineral aerosol (Myhre and Stordal, 2001; Tegen et al., 1996). The modeling study by Lubin et al. (2002) showed that the aerosol IR radiative forcing could be as much as 15% of the large, anthropogenic short-wave forcing found over the Arabian Sea during the Indian Ocean Experiment (INDOEX) experiment.

In this work we report a combined modeling and observational study of the IR aerosol optical properties and the direct IR radiative forcing from the Aerosol Characterization Experiment in Asia (ACE-Asia). We discuss and compare model results with direct observations of the IR aerosol forcing (Vogelmann et al., 2003). The model is tested on the basis of multifaceted observations including surface chemical and optical aerosol properties, columnar and vertical profiles of aerosol optical properties, and surface longwave and solar radiation fluxes.

2. Observations

The ACE-Asia experiment took place in the spring of 2001 and was designed to study the complex outflow of mineral dust and air pollution from Asia at mid-latitudes. The instruments were located on the NOAA Ship Ronald H. Brown and we sailed from Honolulu, Hawaii to the Sea of Japan. On the Pacific transect we were able to observe passages of extra-tropical cyclones and long-range pollution transport. The sampling near the Asian coast found both pollution and dust from the arid regions of Asia.

The total infrared radiative fluxes (3.5-50 μm) were obtained using the broadband, hemispheric view, precision IR radiometer pyrgeometer (PIR, Eppley). According to the technical specifications provided by the manufacturer this instrument has an absolute accuracy of ±2 %. Two handheld Microtops II (Sunphotometer and Ozonometer) (Morys et al., 2001) with spectral filters for visible and near-infrared (NIR) wavelengths were used to retrieve the aerosol optical thickness (AOT), columnar water vapor, and columnar ozone. The AOT was measured at 380, 440, 500, 675, 870 nm by the Sunphotometer and at 1020nm by the Ozonometer. The total water column was obtained from the sun radiance measured at 936 and 1020 nm. The Microtops instruments were calibrated at the Mauna Loa Observatory

Hawaii, just after the field phase of ACE-Asia and we post-processed the data using the new calibration constants. The absolute accuracy of these instruments is about 2%, but the error in the derived total optical thickness is largest for a low air mass (near solar noon). Therefore, the accuracy of the AOT is about 0.01 at 500 nm.

The Fourier Transform Infrared (FTIR) radiometer (Minnett et al., 2001) measured the sky radiance during the cruise and its design is based on the Atmospheric Emitted Radiance Interferometer (AERI) (Revercomb et al., 1988).

The Marine-AERI (M-AERI) measures the sky radiance from 520 to 3020 cm^{-1} (about 18 to 3 μm) at ~0.5 cm^{-1} resolution. Vogelmann *et al* (2003) developed a methodology that determined the IR aerosol forcing in the 10μm window from the M-AERI measurements. We use these observations here to test our aerosol IR model.

Vertical profiles of the aerosol extinction coefficient at 523 nm were measured by a micropulse lidar (MPL) (Welton et al., 2000). The vertical resolution of this instrument is 75m. The aerosol extinction coefficient was obtained from the calibrated lidar signal assuming an altitude-independent backscatter to extinction ratio. NOAA's Pacific Marine Environmental Laboratory (PMEL) determined concentrations of chemical components in the sub- and supermicron size ranges. The analyzed components include sea salt, sulfate, nitrate, total organic carbon, elemental carbon, and dust. "Submicron" and "supermicron" refer to all particles with aerodynamic diameters less than 1 μm and between 1 and 10 μm, respectively, at 55% RH. The methodology of the chemical analysis is described elsewhere c.f. (Quinn et al., 2001; Quinn et al., 2002). We divided the chemical species into several groups according to their physical properties: sulfate and nitrate aerosol mass, sea-salt mass, total organic carbon, elemental carbon, and dust. The concentration of dust was derived assuming that all elements were in their common oxide form (Malm et al., 1994). The particulate organic matter (POM) was determined from the measured organic carbon concentration and the expression POM=2.1xOC (μg Cm^{-3}) (Turpin and Lim, 2001). On the basis of these mass concentrations, we associated the optical properties with these chemical components.

The top-of-atmosphere (TOA) infrared fluxes were obtained from the CERES instrument on board the TERRA satellite (the resolution of CERES is 20 km at nadir). CERES measures radiances, which are converted to fluxes using angular distribution models (Loeb and Kato, 2002). In this study we use Beta 2 SSF CERES data.

3. Aerosol model

The IR radiative aerosol forcing is obtained from radiative transfer calculations (Modtran version 4.1). We use an aerosol optical model based on chemical measurements. We developed a new optical aerosol properties model which offers more flexibility over the OPAC/GADS software which was used previously (Markowicz et al., 2003). In short, the current version offers the advantage that the optical properties such as extinction, absorption coefficient, and the asymmetry parameter are recalculated from Mie theory (Bohren and Huffman, 1983) rather than taken from fixed tables and the choice of size distribution parameters is more flexible. We define seven aerosol types: water-soluble, soot, sea salt accumulation and coarse modes, mineral dust accumulation and coarse modes and sulfate. The "soluble" categories are: (a) nitrate and POM, and (b) sulfates (they differ because

different humidity growth factors are assumed). The "soot" category includes elemental carbon. The mass of the "dust" category is defined as Mass=2.2Al+2.49Si+1.63Ca+2.42Fe+1.94Ti with numerical factors adjusted such that the major elements in dust are converted to their common oxide form (Malm et al., 1994).

We assume that the aerosol components are an external mixture and we perform the Mie computations separately for all 7 types of aerosols. The refractive index of aerosols between 0.25 and 40 μm was used from the Optical Properties of Aerosol and Clouds software (OPAC 3.1) (Hess et al., 1998) and HAWKS 2000 (Rothman et al., 1998) aerosol information part. To account for water vapor intake, the complex refractive index of the medium must be modified by mixing it with the refractive index of water. The effective refractive index for the hygroscopic type of aerosols (soluble and sea salt) are obtained from the Maxwell-Garnett mixing rule (Chylek et al., 1988).

We used the lognormal size distribution to describe the particle optical properties. The soluble, soot, and sulfate types of aerosols (which are generally small) are defined by only one single lognormal size distribution. The sea salt and dust particles are described by two lognormal size distributions (accumulation and coarse mode). However, we have aerosol mass density measurements for both submicron ($r < 0.5$ um) and supermicron ($0.5\ \mu m \leq r \leq 5.0\ \mu m$) particles. In the case of (assumed) single mode distribution, we calculate the equivalent mode radius (Table 1) and number of particles on the basis of these two measured masses and the assumed width of the size distribution (σ) based on the OPAC/GADS data base (Table 1). For the sea salt and dust we use two lognormal distributions and have to assume mode radius for the fine and coarse fractions (Table 1) and calculate the number of particles from the submicron and supermicron mass measurement.

Table 1. Mode radius (r_m) and width σ of the lognormal size distribution

			Sea salt		dust		
	soluble	soot	fine	coarse	fine	coarse	sulfate
r_m	0.03-0.075	0.011	0.10	1.75	0.15	1.9	0.02-0.1
σ	2.24	2.00	2.03	2.03	1.95	2.15	2.03

For the given dry aerosol mass density (_g m^{-3}) in each category we assume a growth factor (Hanel and Zankl, 1979) and calculate the aerosol mode radius at 55% RH. It is this modified radius, which is used to define masses in accumulation and coarse modes. In summary, we obtain the number of particles and mode radii for all 7 types of aerosols.

The aerosol chemical composition is assumed to be constant with altitude to 3km but the vertical optical properties change with height because of the humidity variability. In the upper layer (above 3km), the aerosol optical model includes only dust particles, which is consistent with the numerical simulations performed by the COAMPS/Navy Transport Model and MPL lidar observations, which show layered dust structure for YD99 onwards. The optical thickness and vertical structure of these two layers were obtained from the MPL lidar measurements at 523nm. The spectral extinction coefficient, single scattering albedo, and asymmetry parameter at 62 wavelengths for these two layers were calculated using our optical properties package described above. From the vertical profile of relative humidity (atmospheric soundings from ship were available approximately every 3 hours) and the lidar profiles of aerosol optical thickness we define the mean relative humidity in the two layers. These spectral optical properties were used in the radiative transfer model calculation.

4. Results

(a) Broadband fluxes

Radiative transfer calculations are based on chemical measurements, lidar extinction observations, atmospheric soundings, Microtops aerosol optical thickness (AOT) data, and columnar ozone. We performed model calculations for 81 cases corresponding to the Microtops observations. All of the AOT measurements were performed under clear sky conditions although small cloud fraction is possible outside the solar aureole.

Fig. 1 shows the downward longwave radiation (3.5-50 μm) at the surface during the cruise. The solid line corresponds to pyrgeometer observations and open circles mark radiative transfer model results. High values of fluxes are correlated with the cloudy conditions and large relative humidity. Notice that the model results define the minimal envelope of the pyrgeometer observations associated with the clear sky conditions. For example, after the stormy night on YD85, we measured visible AOT as high as 0.45 which correlates with a small longwave flux (275-285 Wm^{-2}), which indicates non-cloudy conditions.

The agreement between the model and the pyrgeometer is better quantified on Fig. 2a. The radiative transfer model underestimates the total downward fluxes by 2.9 Wm^{-2} (Fig. 2a). In spite of a relatively large rms (7.3 Wm^{-2}) the modeled fluxes can be considered in good agreement with the measurements. The total columnar water significantly influences the difference between observations and model results, partially because soundings were only available, at best, every 3 hours (no attempt was made to use FTIR retrieved soundings in this work).

We used the CERES observations (on the TERRA satellite) to compare fluxes at the TOA. The satellite observation footprint and ship position were collocated with a maximum deviation of 25 km. We chose only data for which the viewing angle was less then 60 degrees. Fig. 2b shows a comparison of modeled and CERES outgoing longwave radiance in the atmospheric window (8-12 μm) at the TOA. We have only 5 days with the cloud free conditions. For TOA the model overestimated the satellite data by 1.7 Wm^{-2}. The difference between model and observations is positive and has a smaller rms (1.9 Wm^{-2}). Possible error sources are the angular distribution model (ADM) specifications (Loeb and Kato, 2002), which are used to convert radiances to fluxes in the SSF CERES data and uncertainties in the aerosol optical model specifications. Model calculations of fluxes in the atmospheric window at the TOA show that the outgoing longwave flux is largely independent of the total column water vapor and, therefore, the TOA flux from CERES can be used to estimate the IR aerosol forcing.

(b) The infrared aerosol-optical properties

In this section we consider the infrared radiation in the atmospheric window between 8-12 μm. As usual, aerosol properties are depend on the refractive index and the aerosol size

longwave radiation. For these particles their single scattering properties are determined by the transition between the Rayleigh and Mie regimes (size parameter $x > 0.3$). Because the extinction efficiency is small for $x \approx 0.3$, and because there are not many large aerosol particles, the infrared extinction is small in comparison to the visible extinction. During the ACE-Asia the number of particles in the sea salt coarse mode varied between 0.005 to 0.38 in cm^{-3} and number of dust particles in coarse mode varied between 0.01-0.63 cm^{-3} (remember that these are derived concentrations and that they can possibly contain contributions from various errors).

Using the aerosol optical model, the vertical profile of extinction coefficient from MPL lidar observations and the aerosol optical thickness at 500 nm we obtained the aerosol optical properties in the infrared atmospheric window. Fig. 3a shows a high temporal variation of the infrared aerosol optical thickness during the cruise. The solid line and open squares on Fig. 3a correspond to the total IR aerosol optical thickness and open circles mark optical thickness calculated without dust contribution. The mean value of the infrared AOT is 0.08 (±0.07) and it is five times smaller than the AOT observed at 500 nm (Markowicz et al., 2003). Lower values (between 0.03 and 0.05) of the infrared AOT in the first part of the cruise were associated with the clean marine air masses of the central and western Pacific Ocean. Only during YD85, after the frontal passage, infrared AOT increased to about 0.18 in the morning, and 0.13 later that afternoon. The visible to the infrared AOT ratio was approximately 2.5, which is relatively small and due to the increase in large particle concentration. For that case we observed a flat spectral AOT (small Ångstrom exponent) in the visible and near infrared. The Ångstrom exponent evaluated for 500 and 870 nm is shown in Fig. 4a for the ACE-Asia cruise. Small values over the central Pacific Ocean correspond to clean marine air masses with small fraction of submicron particles. Between YD97 and YD103, a mineral dust with aloft had significant influence on the optical properties of aerosol as seen by the small Ångstrom exponent.

Between YD98 and YD99 the infrared AOT increased strongly which correlates with the dust layers in the middle troposphere. Throughout YD99 the infrared AOT is 0.25 while the visible value is about 1. From YD99 onwards the layer of dust was descending and on YD102 the situation was dominated by dust in the boundary layer. The number of dust particles in the coarse mode inferred from chemical measurements at the surface is about 0.6 cm^{-3}. The infrared AOT was 0.15 in the morning and decreased to 0.1 later that afternoon. These results correlate with the visible AOT and the dust concentration at the surface. During the last days of the cruise the infrared AOT was small with the exception of YD107 when it increased to 0.13.

The variability of the no-dust IR optical thickness (open circles) was much smaller than the total IR optical thickness and usually smaller than 0.05 with the exception of YD85. During the days with dust it contributed about 20% to the total IR optical thickness.

Overall the correlation coefficient between the infrared AOT and visible (500 nm) AOT is 0.82 (Fig. 4b). If spite of the significant correlation we cannot estimate the infrared AOT based on just one visible measurement. However, the multi-spectral observations by the sunphotometer include information about columnar size distribution. For example, the Ångstrom exponent defined for two wavelengths is a function of the ratio particle concentration in the accumulation and the coarse mode. Therefore during days with high infrared AOT we measured low value of Ångstrom exponent. Moreover during these days correlation of the infrared AOT and visible AOT is much better (Fig. 4b).

The columnar infrared single scattering albedo (SSA), defined as extinction-weighted SSA, at 10 μm is shown in Fig. 3b. The SSA varies from 0.4 to 0.7, thus the scattering of radiation in the atmospheric window is appreciable. The highest values of the SSA (0.65-0.7) were observed in the first part of the cruise and correspond to almost conservative SSA in the

visible. The correlation between visible and infrared SSA is poor, (r^2=0.66) although the general trend of these two quantities (not presented) is similar. One important reason for such a small correlation is the presence of water vapor. In the visible, the increase of RH leads to an increase of SSA while in the infrared atmospheric window the imaginary part of the refractive index of water is large and the increase of RH correlates with an increase of absorption (smaller SSA). Over the Sea of Japan, the infrared SSA is smaller in comparison to the Pacific transect and during the dust events the infrared SSA is between 0.45 - 0.5.

There were no direct measurements of the SSA in the infrared. However, the measured surface SSA at 550nm compares well with the modeling results (Markowicz et al., 2003) in the visible which provides a certain degree of confidence about the validity of our optical model. The aerosol refractive index and size distribution of particles are the source of uncertainties in derivation of the infrared SSA. This is particularly true about mineral dust. The mineral dust refractive index changes significantly with its composition (Sokolik et al., 1998). However, in this study we used the refractive index of dust available in the OPAC/GADS database. We validate our optical model against available measurements of extensive parameters (fluxes). Also, the size distribution changes lead to large changes of the infrared SSA. The Fig. 5 shows SSA as a function of a size parameter ($x=2\pi r/\_$) based on the effective radius. The three lines on this figure correspond to different imaginary parts of the refractive index. The dotted line corresponds to $k=10^{-3}$, the solid line to $k=10^{-2}$, and the dash-dotted line corresponds to $k=10^{-1}$. In the infrared (8-12 μm) part of the spectrum the size parameter is usually less than $x_{eff} < 1$ and the SSA is, therefore, a strong function of the effective radius. The decrease of particle radius leads to a decrease of the SSA and a change of the surface and TOA infrared aerosol forcing. Also one can infer from that small particles (fine mode) are black in the infrared and, therefore, only large particles can effectively scatter radiation.

(c) Infrared aerosol forcing

In this section we derive the longwave radiative aerosol forcing at the surface and at the top of the atmosphere (TOA). At the surface, the forcing is defined as the difference between downward longwave flux with the aerosol and without the aerosol. In contrast to the solar region (where the Sun is the source of energy from space and even small backscatter can cause a negative aerosol forcing) the infrared aerosol forcing at the surface is always positive. This is caused by the additional downward flux from the aerosol layers. At the top of the atmosphere the outgoing longwave radiation (OLR) is, in most cases, decreased by the aerosols, except for strong inversion cases when the temperature of the aerosol is higher than the surface temperature. To determine the aerosol forcing we perform two radiative transfer calculations with and without aerosols in the atmosphere.

The effect of aerosols on longwave radiation is significant only in the atmospheric window, where the absorption by gases (mostly water vapor and carbon dioxide) is small. Therefore, we present model results in the atmospheric window range (8-12 μm). We compare these model results with the aerosol forcing obtained from mode detailed observations based on M-AERI (Vogelmann et al., 2003). The M-AERI measured spectra contain the combined downward emissions by aerosols and greenhouse gases (e.g., H_2O, CO_2). The aerosol's radiative effect was obtained by removing the contribution of gaseous emission using a modeled, aerosol-free spectrum. The aerosol radiance effect was converted to an aerosol IR radiative forcing using a radiance-to-flux conversion. The clean-sky spectra were computed using the Line-By-Line Radiative Transfer Model LBLRTM. In Vogelman *et al.* (2002) the water vapor and temperature profiles are specified every 10 min using M-AERI

retrievals for the lowest 3 km and, above that, the nearest radiosonde launched from the ship whereas in this work we used only the radiosonde data.

The general comparison of the surface infrared aerosol forcing obtained from M-AERI and from our radiative transfer model is shown in Fig. 6. Although the differences between model and observations are small (0.5 Wm^{-2}) the rms is relatively large 1.6 Wm^{-2}. Let us recall that the model calculations are based on surface optical properties derived from the chemical characterization of the aerosol and the vertical extinction profile derived from lidar and visible AOT at 500nm. Possible discrepancies between the M-AERI and the model results reported here may be related to the fact that the surface chemistry is not representative for the lower troposphere and that dust properties are not modeled properly. Also, the lidar extinction algorithm is source of error. However, the overall comparison is good and many features are resolved by our model as is illustrated in Fig. 7. This provides additional validation for the aerosol-optical properties choice. In the central part of Pacific Ocean the longwave surface forcing is small and equal to about 1 Wm^{-2} with the exception of YD85. For comparison, the solar aerosol forcing in this region is -5 Wm^{-2} (Markowicz et al., 2003). During YD85 the longwave aerosol forcing increased and in the morning was about 6 Wm^{-2} decreasing to about 4.5 Wm^{-2}in the late afternoon. The mean solar aerosol forcing on YD85 was -22 Wm^{-2}. The GOCART model (Mian Chin, private communication, results not presented) shows dust in the boundary layer for that day. This indicates that combined effect of the sea salt close to surface and dust in the boundary layer has an important effect on radiation in both solar and infrared and leads to a strong cooling at the surface. Between YD86 and YD99 the infrared forcing slowly increased to over 2 Wm^{-2}. The maximum aerosol forcing observed on YD99 and YD100 (8-10 Wm^{-2}) is associated with the dust layer in the middle troposphere. For these days the surface aerosol forcing in the solar region is about 5 times larger (absolute value) than in the infrared forcing. The infrared forcing for YD99 and YD102 are similar but their AOTs (both in solar and IR) are different. This is because on YD99 the dust was between 5-10km, and on YD102 it was closer to surface, thus, the temperature effect of the warmer dust compensated for its smaller optical depth.

The longwave TOA aerosol forcing is obtained from the radiative transfer model and CERES data (only 5 clear days). The TOA forcing is estimated by subtracting the clear (without aerosol) outgoing flux in the atmospheric window obtained from the radiative transfer model and the flux measured by the CERES instrument. After plotting the infrared forcing as a function of the infrared AOT we noticed a bias for small AOTs, of approximately 0.9 Wm^{-2}. However, on physical grounds, one would not expect any forcing for small AOT. Such a bias may be due to several factors related to clear-sky model imperfections. Guided by the slope technique derived for the solar spectrum forcing calculations (Satheesh and Ramanathan, 2000), we applied the same methodology to remove the bias. Fig. 7b shows the temporal variation of the TOA infrared aerosol forcing. The solid triangles on Fig. 7b show the aerosol forcing at the TOA between YD97 and YD105 obtained from satellite. The open circles are model results. The results are in good agreement with radiative transfer calculations with the exception of YD99. During this day, the aerosol forcing from satellite observations is about 2.5 Wm^{-2} larger than obtained from the model. However, YD99 was misclassified by the satellite algorithm as cloudy probably due to hazy conditions. The largest forcing is about 4.5 Wm^{-2}during YD99 and YD100 and is about two times less than at the surface. Much smaller TOA forcing was observed on YD102 which is due to the previously discussed temperature effect. The TOA aerosol forcing without dust is small and did not exceed 0.5 Wm^{-2} . However, for sea-salt dominated YD85 the TOA longwave forcing is between 1.2 and 1.8 Wm^{-2}. In comparison with the solar spectrum the TOA infrared aerosol forcing is about 4 to 6 times smaller.

The strong correlation between infrared aerosol forcing at the surface and infrared (10 μm) AOT is shown on Fig. 8. The open squares represent cases with upper aerosol layers present and open circles mark all other data. This division is based on the following criterion $(T_A/T_S)^4<1.2$, where T_S is the surface temperature and T_A is the mean aerosol temperature. It can be seen that, in a first approximation, the infrared aerosol forcing is a linear function of the infrared AOT. Let us now define the infrared aerosol forcing efficiency as the ratio of aerosol forcing to infrared AOT. The infrared forcing efficiency is 55 Wm^{-2} (per IR optical depth unit) for the boundary layer aerosol and 37 Wm^{-2} (per IR optical depth unit) in the case of elevated dust. If the aerosols are close to the surface, they cause an increase of the surface forcing but a decrease of the TOA forcing. The TOA aerosol forcing as a function of the infrared AOT is shown on Fig. 9; the forcing efficiency is about 18 Wm^{-2} (per IR optical depth unit) in the case of elevated dust and 10 Wm^{-2} (per IR optical depth unit) when the aerosol is mostly in the boundary layer. This difference of forcing efficiency is due to the emission temperature.

We attempted to derive the radiative forcing using the Eppley broadband, hemispheric field of view pyrgeometer, but the results were unpromising. This is most probably due to several effects: (a) a too broad spectral range (3.5-50μm), (b) the hemispheric field of view (cloud contamination), (c) uncertainty in the water vapor profiles.

5. A Simple Model of Infrared Forcing

In this section we develop a simple 2-stream model to gain insight into the physics of dust forcing. We assume that the aerosol layer is isothermal and that there is no gaseous absorption in the atmospheric window. Neglecting multiple scattering we can write the flux at the top ($F_t^{\uparrow}$) and at the bottom ($F_s^{\downarrow}$) of the aerosol layer as:

$$F_t^{\uparrow} = TF_s^{\uparrow} + F_s^{\uparrow}R^{\uparrow} + \pi AB_a, \quad (1)$$

$$F_s^{\downarrow} = R^{\downarrow}F_s^{\uparrow} + \pi AB_a, \quad (2)$$

where, B_a is the black body irradiance at the temperature of the aerosol layer. Parameters A and T are the aerosol absorption and transmittance, $R^{\uparrow}$ and $R^{\downarrow}$ are up and down reflection coefficients, respectively, subscript "s" stands for "surface" and "a" for "aerosol". In the case of small optical thickness τ, the parameters in equations (1) and (2) can be written as:

$$T = 1-\tau, \quad (3)$$

$$A = \tau(1-\omega), \quad (4)$$

$$R^{\uparrow} = \tau\omega(1-\beta), \quad (5)$$

$$R^{\downarrow} = \tau\omega\beta \quad (6)$$

where ω is a single scattering albedo and β is the backscatter coefficient. The radiative forcing above and below the aerosol layer can be written as:

$$\Delta F_t = \tau F_s^{\uparrow}\left[\left(1-\frac{B_A}{B_S}\right)(1-\omega)+\omega\beta\right], \quad (7)$$

$$\Delta F_s = \tau F_s^{\uparrow}\left[\frac{B_A}{B_S}(1-\omega)+\omega\beta\right] \quad (8)$$

where, B_s is the black body irradiance at the surface temperature. In this simple model the aerosol forcing at the TOA and at the surface is a linear function of the infrared AOT. The first terms in Equations 7 and 8 are associated with the thermal emission by the aerosol layer relative to the surface emission and the second terms are associated with the downward scattered fraction of radiance. For typical values, the terms at the TOA are comparable, while

scattering term. Thus, the TOA infrared aerosol forcing in contrast to the surface aerosol forcing is more sensitive to the aerosol scattering.

The thermal effects at the TOA and at the surface are opposite and are consistent with detailed radiative transfer model calculations (Fig. 8 and Fig. 9). The up scattered backscatter coefficient can be written approximately as $\beta=1/2(1-g)$ (Wiscombe and Grams, 1976). The influence of the backscatter on the infrared aerosol forcing is similar at the TOA and at the surface. In both cases the increase of the backscatter leads to an increase of the aerosol forcing. Thus, smaller particles (small asymmetry parameter) have a larger influence on the aerosol forcing in the infrared due to the scattering effect, which is similar to the solar aerosol forcing. The infrared SSA influences the infrared aerosol forcing in two opposite ways. The decrease of SSA (higher absorption) leads to an increase of the thermal emission by the aerosol layer, but to a decrease of the scattered part of radiation. It follows from Eq. (8) that for

$$\beta < \frac{B_a}{B_s} \tag{9}$$

the decrease of SSA leads to an increase of the infrared aerosol forcing at the surface. This condition is always satisfied, because the backscatter coefficient is less than 0.5 and B_a/B_s ratio is usually between 0.8 and 1. The SSA influence on the TOA aerosol forcing is more complicated. For

$$\frac{B_a}{B_s} < 1-\beta \tag{10}$$

a decrease of SSA leads to an increase of the infrared aerosol forcing at the TOA. Thus, for a constant backscatter coefficient one can always find a temperature at which the TOA aerosol forcing is increasing with increased absorption. For typical atmospheric conditions Eq. (10) may or may not be satisfied. Therefore, the relationship between the infrared TOA forcing and SSA changes depends on relative black body temperatures and the backscatter coefficient. On the other hand, the shortwave TOA forcing always increases with increasing absorption (but even can change sign).

6. The Role of Scattering and Total Water Vapor Content on TOA and Surface Infrared Forcing

By keeping the total aerosol absorption and extinction constant and performing two radiative transfer model (MODTRAN) calculations: (a) with the asymmetry parameter set equal to 1 and (b) asymmetry parameter determined from the aerosol optical model, we can investigate the role of scattering on the infrared aerosol forcing ("scattering"). Upper plot on Fig. 10 corresponds to the surface aerosol forcing and bottom plot corresponds to the TOA forcing. Solid lines are for the asymmetry parameter (g) determined from the aerosol optical model and dotted lines are for g=1. In the last case only forward scattering is possible. Neglecting aerosol scattering leads to underestimate of the surface and TOA IR forcing. Scattering has larger effect on the TOA forcing and this result is consistent with the simple aerosol-forcing model. Neglecting scattering causes the mean error between 20-30%. The surface aerosol forcing decreases about 10-15 % when the backscattering is set to zero. These results are consistent with the model results presented by Dufresne et al. (2002).

To estimate the water vapor effect on IR aerosol forcing we performed additional calculations varying the total water vapor content. Fig. 11 shows the TOA (open circles) and the surface (open squares) aerosol forcing computed on YD99. Increase of total water vapor from 0 g/cm^2 to 3 g/cm^2 leads to large decrease of the surface aerosol forcing by about 50% while it is only 9% at the TOA. The relationship between the total water vapor content on the

water vapor and extinction coefficient. The small influence of water vapor on the infrared TOA indicates that water vapor will play secondary effect on retrieval of the infrared aerosol effect from satellite observations in this case. On the other hand, when examining all cruise data, we did not observe significant correlation between the longwave surface aerosol forcing and the total water vapor in a column because the optical depth and temperature provide the dominant effect.

7. Conclusions

In this paper, the aerosol infrared radiative forcing is studied in detail. On the basis of chemical measurements and optical properties in the visible (MPL lidar and sunphotometer observations) we estimated the infrared aerosol optical thickness, the single scattering albedo, and the asymmetry parameter. The surface model results were compared to more detailed FTIR based observations of Vogelmann et al. (2003). The uncertainty of their method is about $\pm 1 Wm^{-2}$. The rms of the difference between the FTIR and our model calculations is about 1.6 Wm^{-2}. Possible discrepancies may be related to uncertainties in the vertical representations of the chemistry, uncertainties in dust properties, errors in lidar extinction retrievals, and errors in the visible AOT estimate. Despite these errors, the present model properly resolves many features. This combined approach augments the FTIR observational study, validates the optical model, and, thus, provides the opportunity to derive infrared forcing at the TOA and infrared single scattering properties.

We found that the infrared AOT is strongly correlated with the infrared aerosol forcing at the TOA and at the surface. The mean infrared AOT at 10 μm was 0.08 (±0.07) and SSA was 0.55. The infrared aerosol forcing reaches up to 10 Wm^{-2} during the ACE-Asia cruise which is a significant contribution to the total (direct aerosol effect. Fig. 12 shows mean daily solar and longwave aerosol forcing at (a) the surface and (b) the TOA. The surface IR aerosol radiative forcing (Fig. 12a) is between 10 to 25% of the shortwave aerosol forcing. The infrared TOA aerosol forcing is between 1% - 19% of the solar aerosol forcing (Fig. 12b). We were able to compare satellite observations for 5 clear days and obtained good agreement with the atmospheric window derived forcing and the CERES satellite retrievals. Our results show that the negative solar aerosol forcing during days with large AOT (YD99, YD100, YD102) is decreased by the IR forcing by about 20%. Over the Sea of Japan the mean solar forcing during the ACE-Asia was –26.1 Wm^{-2} (Markowicz et al., 2003) and the total Solar-IR radiative forcing was –21.5 Wm^{-2} at the surface. At the TOA the mean shortwave forcing was –12.7 Wm^{-2} and the total was -11.2 Wm^{-2}. For a constant aerosol temperature, the TOA and the surface forcing are linear functions of the infrared AOT. We define the infrared forcing efficiency as useful parameter to describe the aerosol effects at the TOA and at the Earth's surface. The TOA forcing efficiency is a strong function of the aerosol layer temperature and changes between 10 to 18 Wm^{-2} (per unit of optical depth) while the surface forcing efficiency varied between 37 and 55 Wm^{-2} (per unit of optical depth). For comparison, the solar aerosol forcing efficiency over the Sea of Japan was –27 Wm^{-2} (per unit of optical depth) and -58 Wm^{-2} (per unit of optical depth), respectively, at the TOA and at the surface.

Acknowledgments.

KMM was supported by a junior Fulbright grant.

PJF was supported by the

PE0602435N. AMV was supported by the National Science Foundation (ATM-0109135) grant. We would like to thank Joao Teixeira for his comments. Dave Bates collected lidar data during the R/V Ronald H. Brown cruise.

Figures

Fig. 1 Downward longwave flux (3.5 - 50 μm) at the surface as a function of Year Day. The solid line represents pyrgeometer observation and the open circles mark model results.

Fig. 2 Comparison of measured and modeled (a) downward fluxes at the surface between 3.5 and 50 μm, and (b) outgoing fluxes at the TOA in the atmospheric window (8-12 μm).

Fig. 3 Temporal variation of (a) total (open squares and solid line) and no-dust (open circles) aerosol optical thickness (AOT) at 10 μm, and (b) vertically averaged infrared single scattering albedo (SSA) at 10 μm during the ACE-Asia cruise.

Fig. 4. (a) Ångstrom exponent and (b) infrared (at 10 μm) aerosol optical thickness as a function of the visible (at 0.5 μm) aerosol optical thickness.

Fig. 5 Single scattering albedo (SSA) as function of size parameter based on size distribution effective radius. The dotted line corresponds to (constant with wavelength) refractive index $n=1.5-i10^{-3}$, the solid line is for $n=1.5-i10^{-2}$, and the dash-dotted line is for $n=1.5-i10^{-1}$.

Fig. 6 Comparison of longwave aerosol forcing at the surface obtained from radiative transfer model and FTIR observations. Solid line corresponds to perfect agreement.

Fig. 7 (a) Surface and (b) the TOA infrared aerosol forcing as a function of Year Day. The open circles represent radiative transfer model results and the solid triangles define the TOA forcing obtained from the FTIR observations (a) and TERRA satellite CERES data (b). The asterisk shows the misclassified point by the satellite algorithm.

Fig. 8 The longwave aerosol forcing at the surface as function of infrared AOT. Square points represent aerosol forcing during the upper layer event and open circles are for all other days. The upper layer dust events was classified on the basis of surface and aerosol temperatures $(T_s/T_a)^4>1.2$.

Fig. 9 Same as Fig. 8 but for the TOA aerosol forcing

Fig. 10 The surface (a) and the TOA aerosol IR forcing as a function of the Year Day. Computation is either exact (solid line) or neglects scattering (dotted line).

Fig. 11 The TOA (open circles) and the surface (open squares) aerosol forcing as a function of the total water vapor content.

Fig. 12 Comparison between (a) the surface and (b) the TOA shortwave and IR aerosol forcing. The positive values correspond with the IR forcing and negative values are for the solar aerosol forcing.

Fig. 1

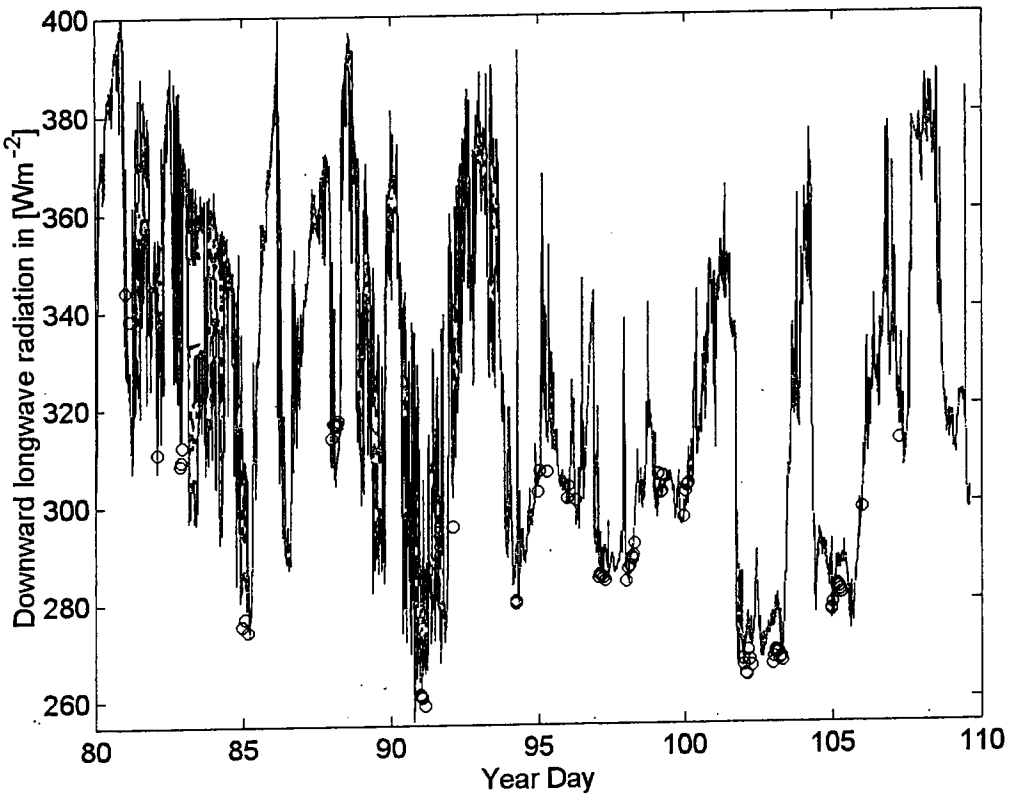
Downward longwave radiation in [Wm^{-2}]
400
380
360
340
320
300
280
260
80
85
90
95
100
105
110
Year Day

Fig. 2

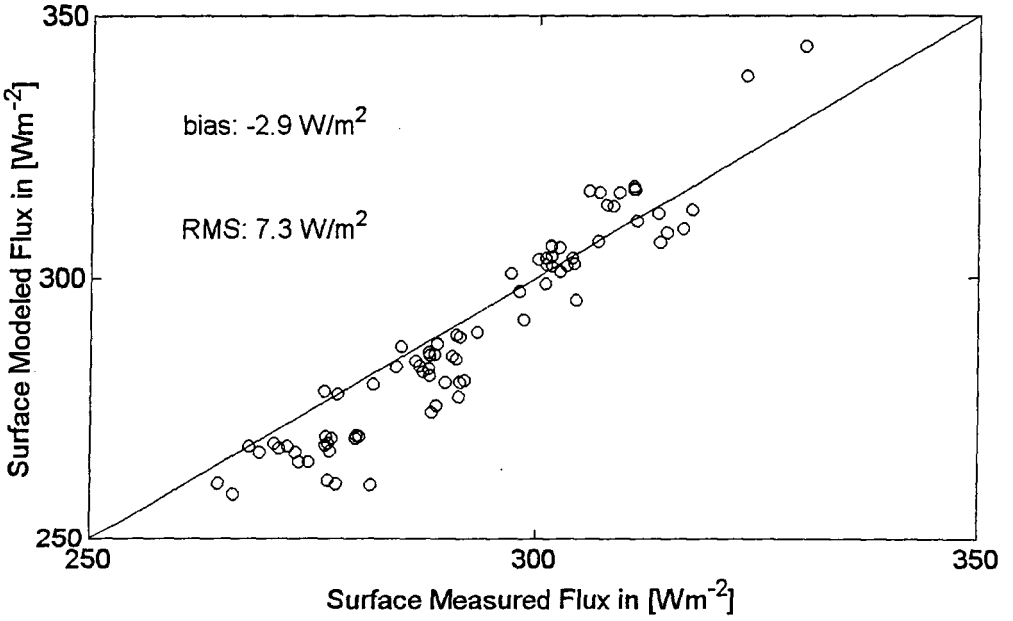
350
300
250
250
300
350
bias: -2.9 W/m2
RMS: 7.3 W/m2
Surface Modeled Flux in [Wm-2]
Surface Measured Flux in [Wm-2]

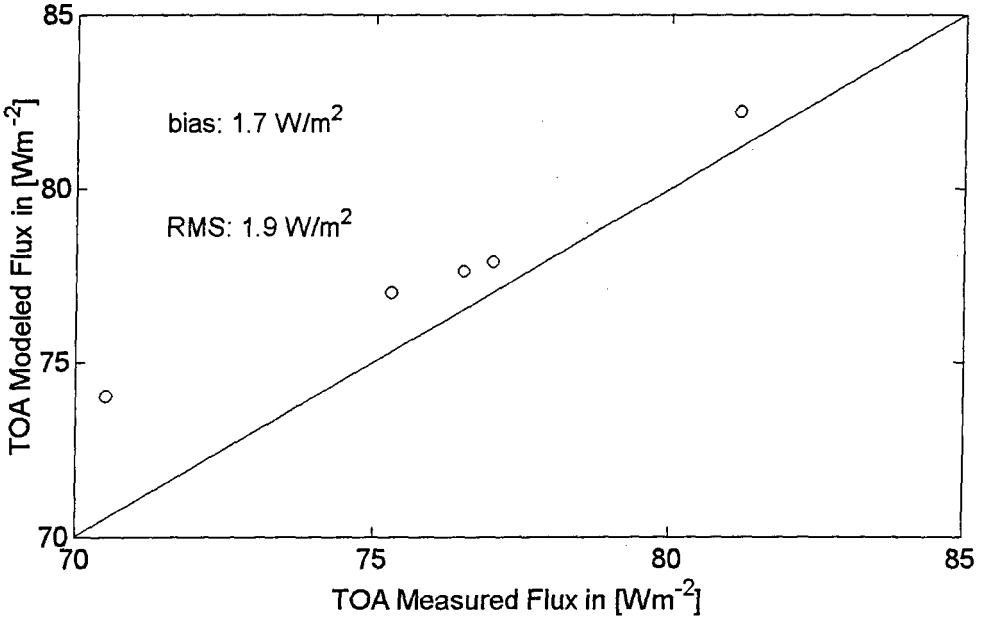
85
80
75
70
70
75
80
85
bias: 1.7 W/m2
RMS: 1.9 W/m2
TOA Modeled Flux in [Wm-2]
TOA Measured Flux in [Wm-2]

Fig. 3

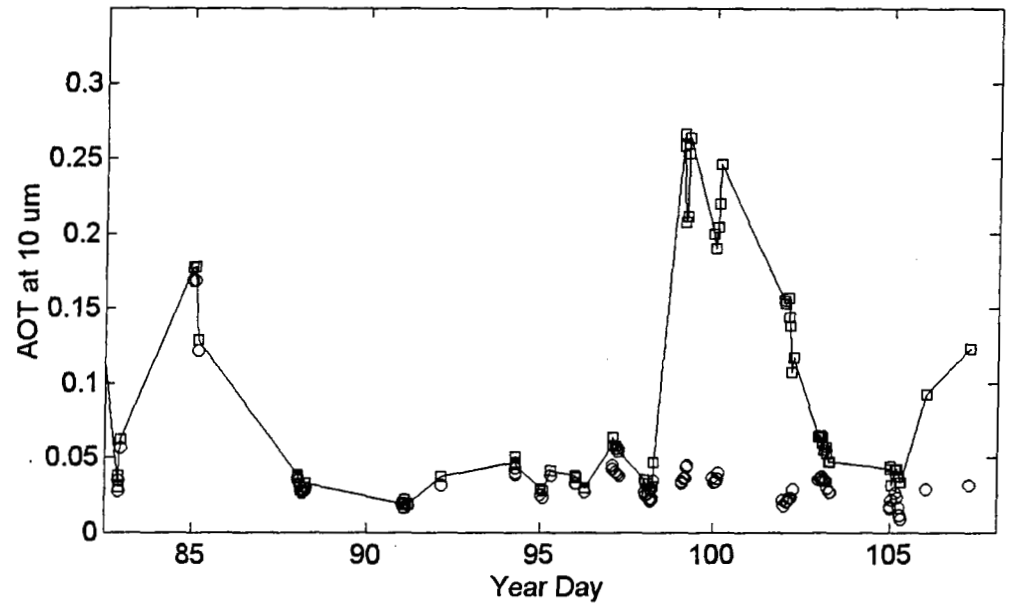
AOT at 10 um
0.3
0.25
0.2
0.15
0.1
0.05
0
85
90
95
100
105
Year Day

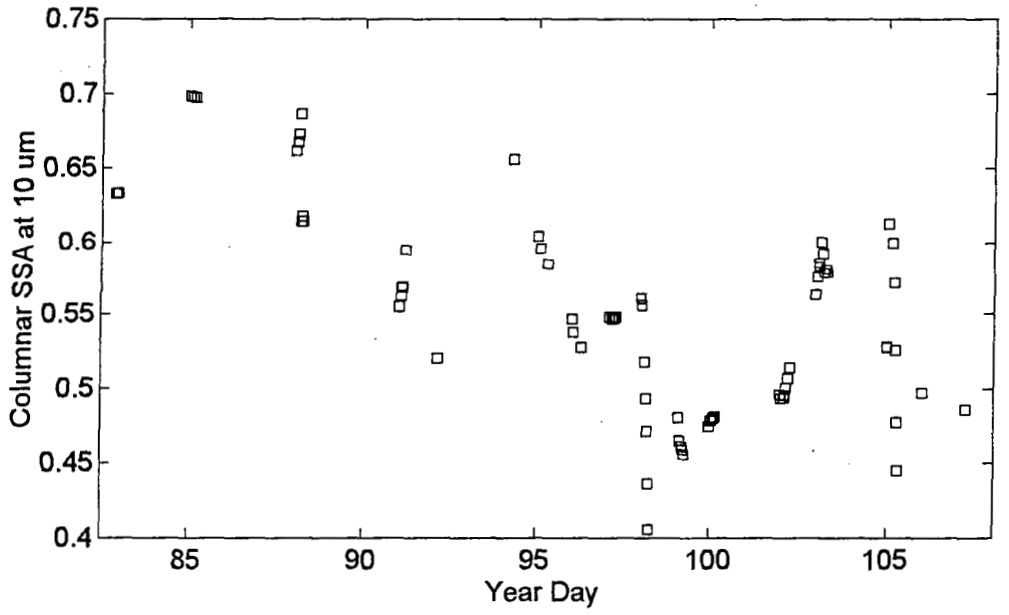
Columnar SSA at 10 um
0.75
0.7
0.65
0.6
0.55
0.5
0.45
0.4
85
90
95
100
105
Year Day

Fig. 4

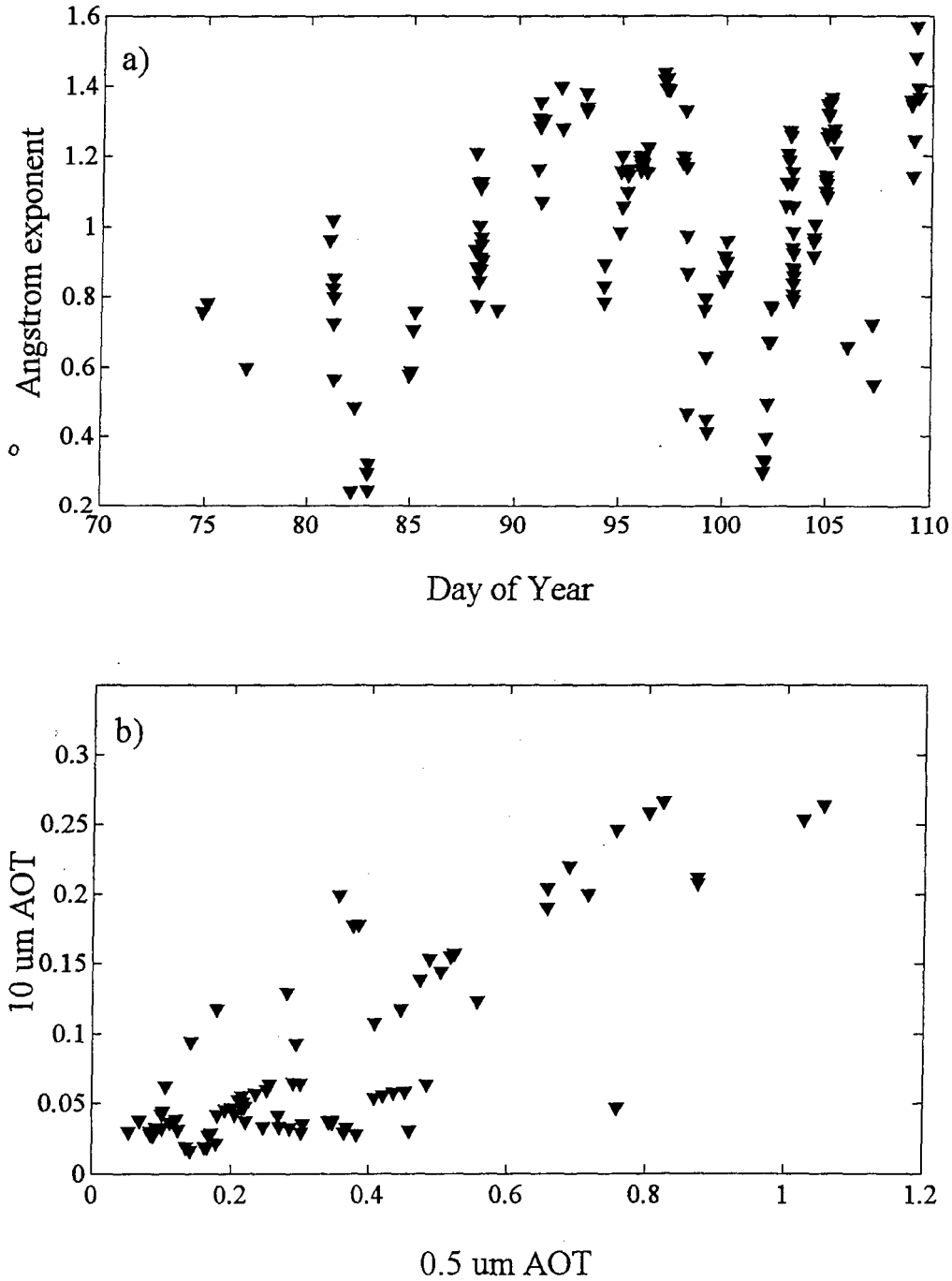
a)
Angstrom exponent
1.6
1.4
1.2
1
0.8
0.6
0.4
0.2
70
75
80
85
90
95
100
105
110
Day of Year
b)
10 um AOT
0.3
0.25
0.2
0.15
0.1
0.05
0
0
0.2
0.4
0.6
0.8
1
1.2
0.5 um AOT

Fig. 5

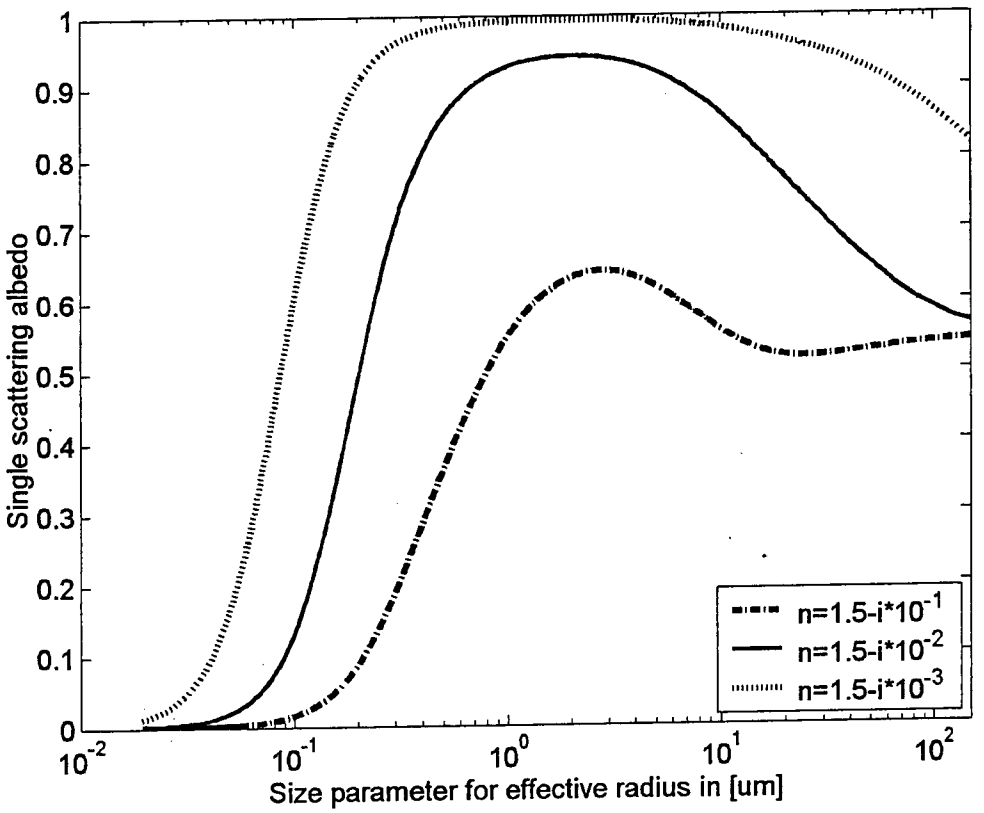
Single scattering albedo
Size parameter for effective radius in [um]
n=1.5-i*10^-1
n=1.5-i*10^-2
n=1.5-i*10^-3

Fig. 6

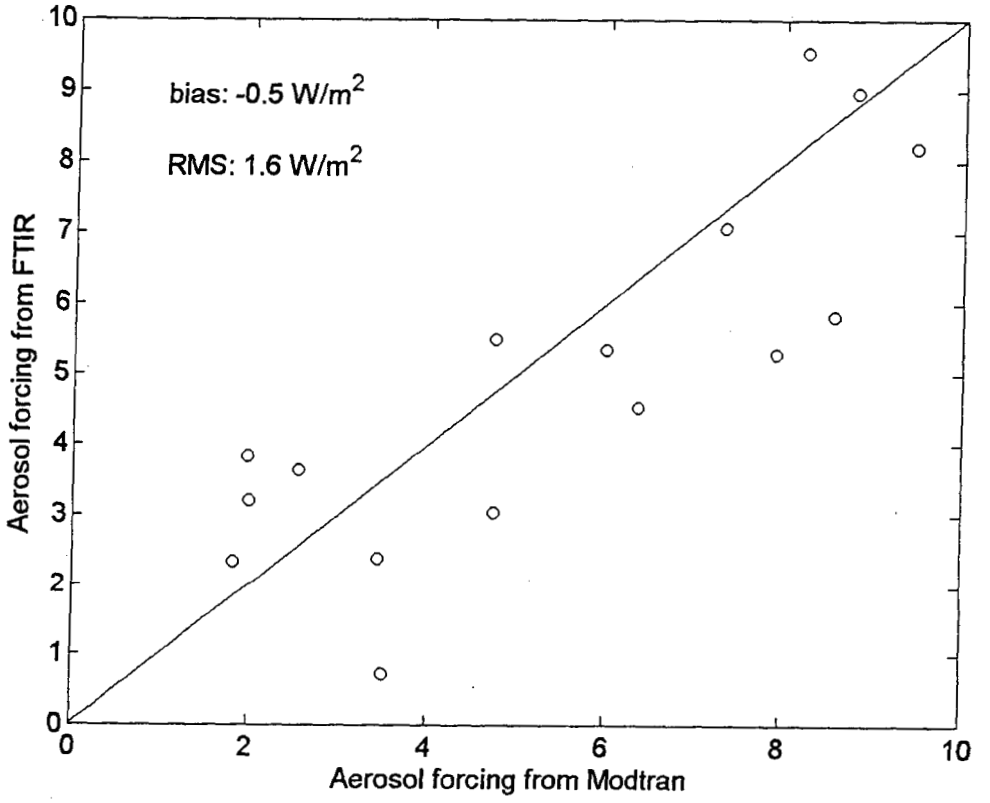
bias: -0.5 W/m2
RMS: 1.6 W/m2
Aerosol forcing from FTIR
Aerosol forcing from Modtran
0
1
2
3
4
5
6
7
8
9
10
0
2
4
6
8
10

Fig. 7

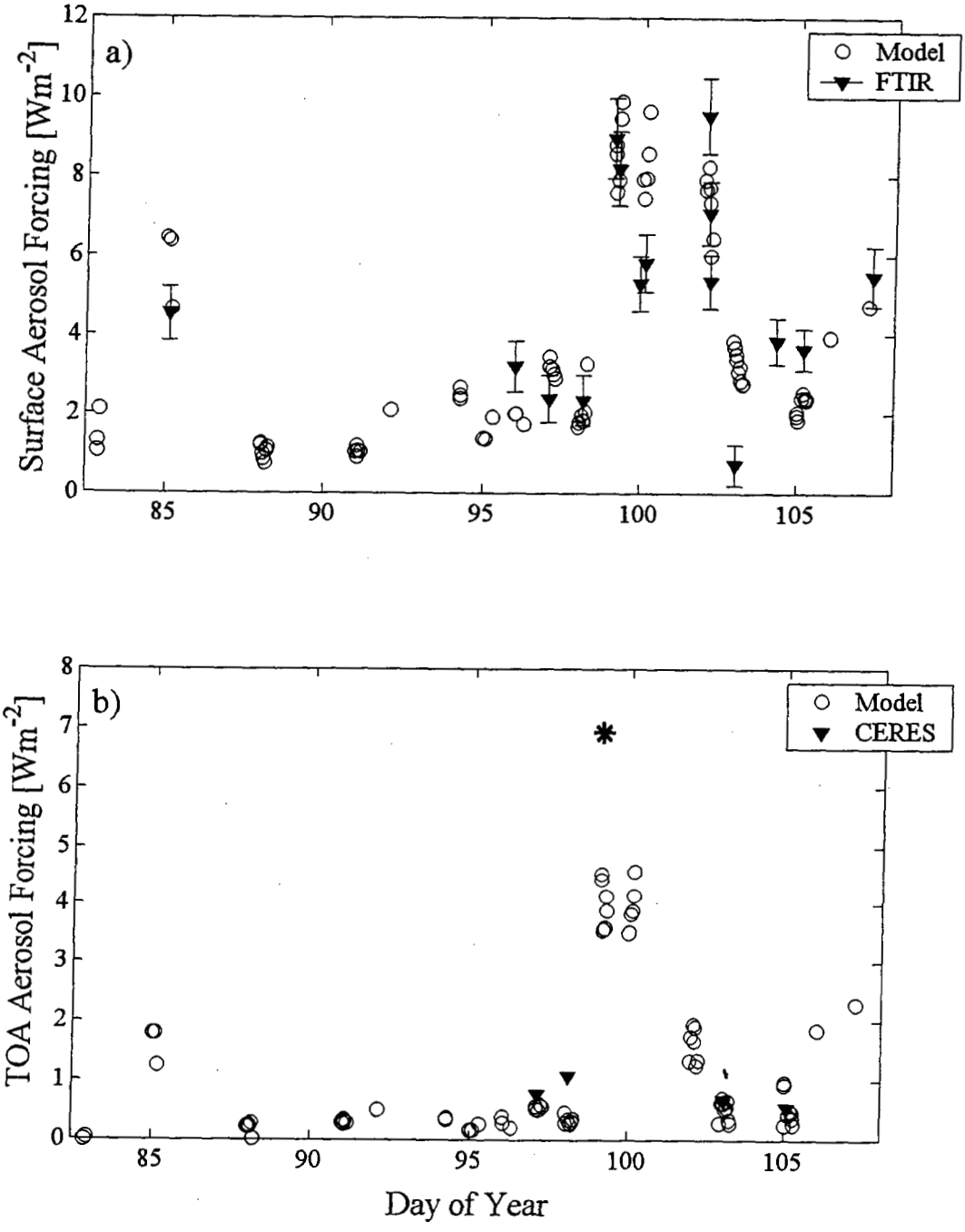
a)
Model
FTIR
Surface Aerosol Forcing [Wm-2]
0
2
4
6
8
10
12
85
90
95
100
105
b)
Model
CERES
TOA Aerosol Forcing [Wm-2]
0
1
2
3
4
5
6
7
8
85
90
95
100
105
Day of Year

Fig. 8

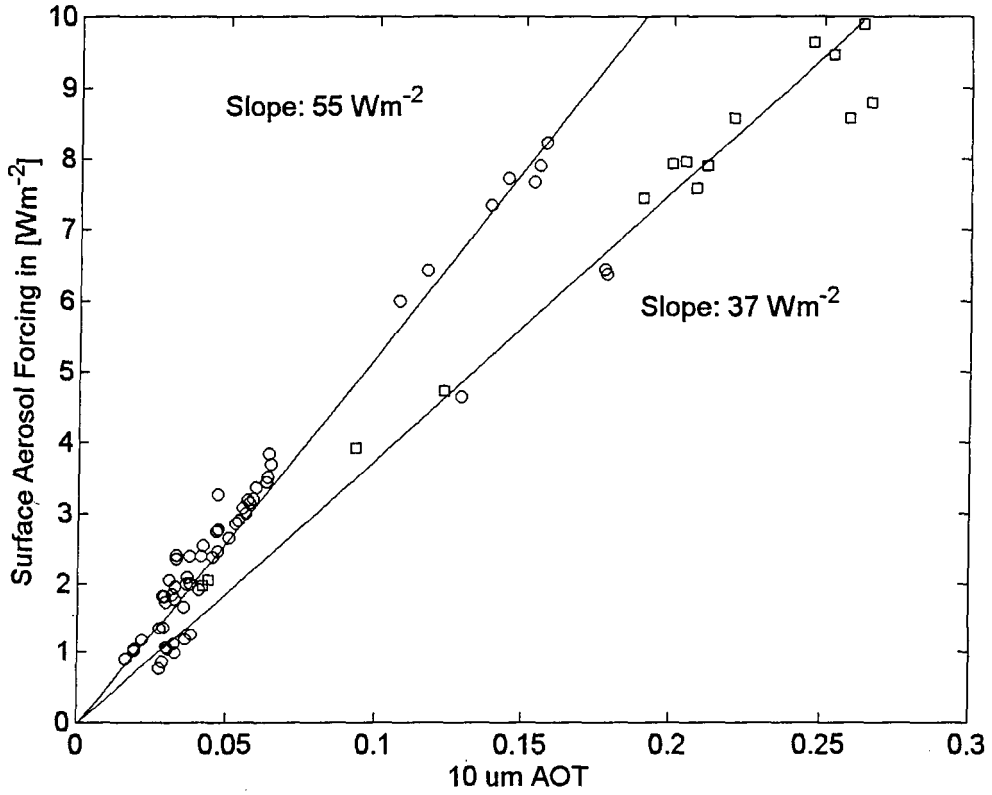
Slope: 55 Wm-2
Slope: 37 Wm-2
Surface Aerosol Forcing in [Wm-2]
10 um AOT
0
1
2
3
4
5
6
7
8
9
10
0.05
0.1
0.15
0.2
0.25
0.3

Fig. 9

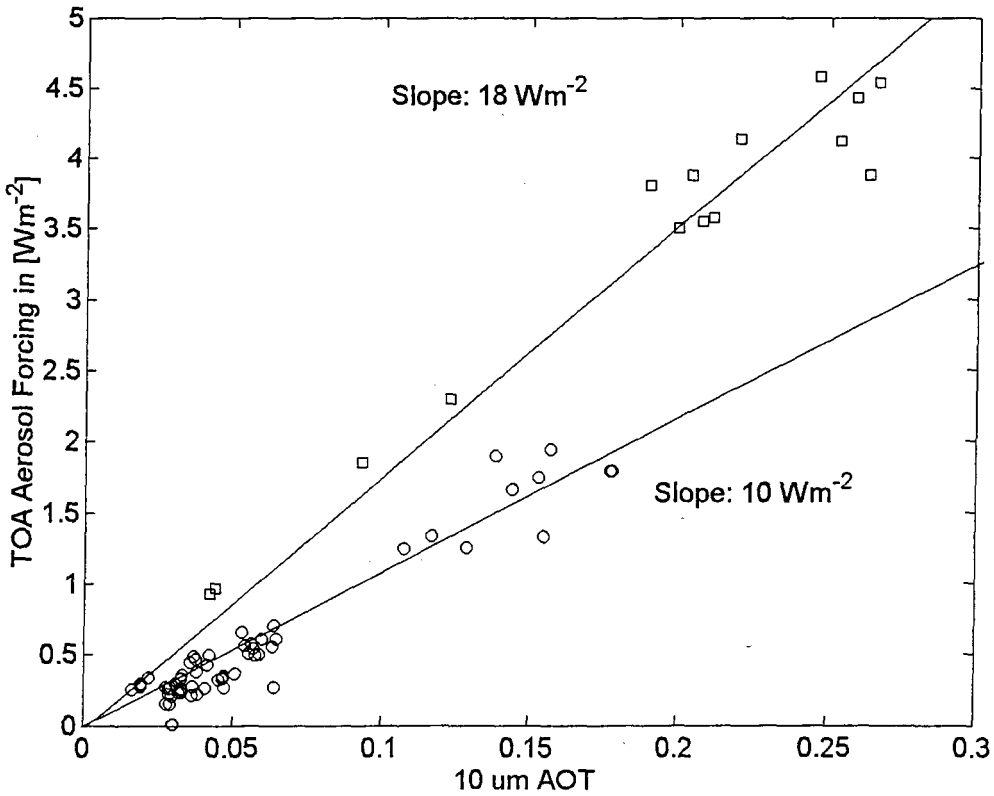
Slope: 18 Wm-2
Slope: 10 Wm-2
TOA Aerosol Forcing in [Wm-2]
10 um AOT
0
0.5
1
1.5
2
2.5
3
3.5
4
4.5
5
0.05
0.1
0.15
0.2
0.25
0.3

Fig. 10

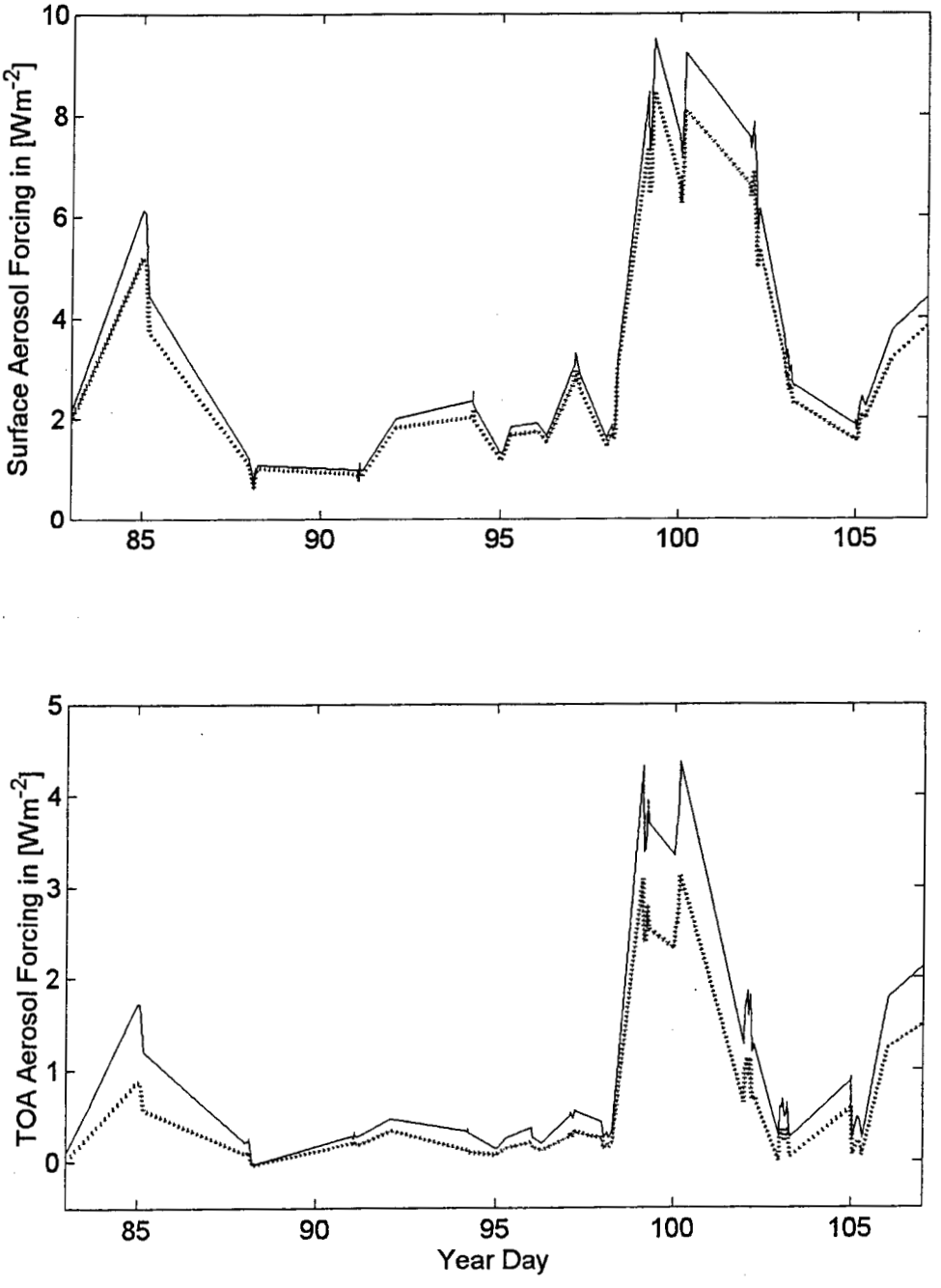
Surface Aerosol Forcing in [Wm-2]
10
8
6
4
2
0
85
90
95
100
105
TOA Aerosol Forcing in [Wm-2]
5
4
3
2
1
0
85
90
95
100
105
Year Day

Fig. 11

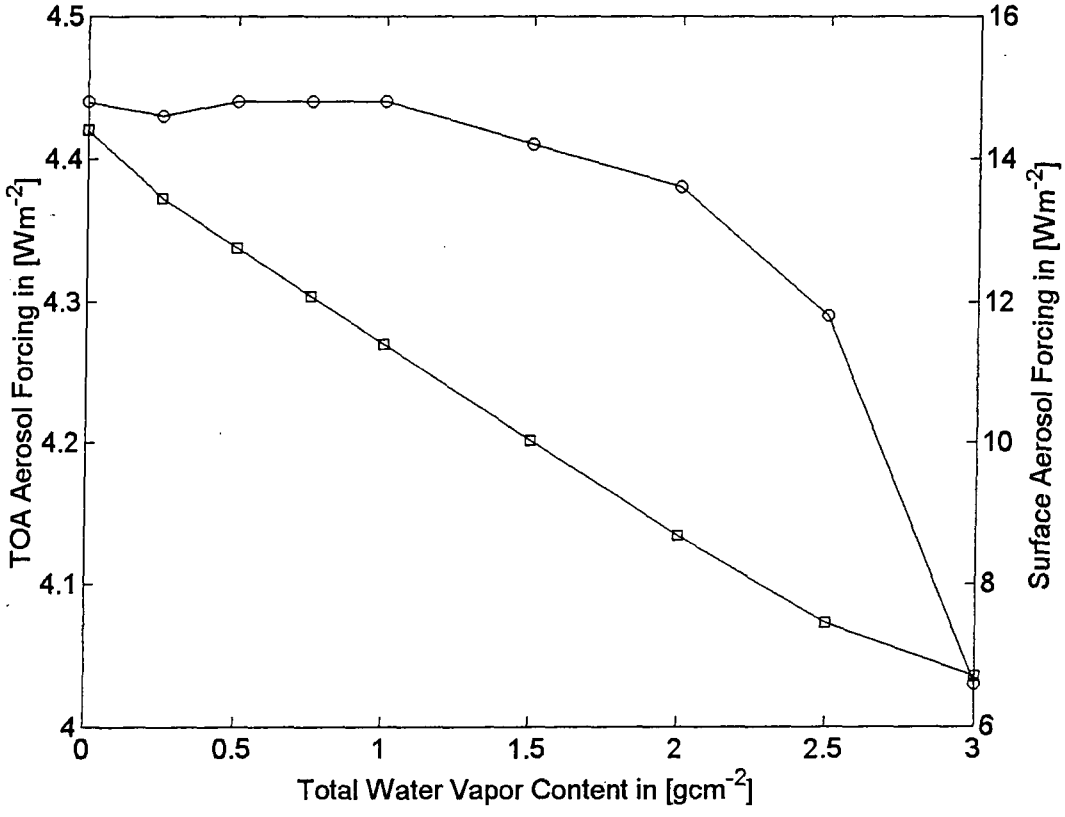
4.5
4.4
4.3
4.2
4.1
4
16
14
12
10
8
6
0
0.5
1
1.5
2
2.5
3
TOA Aerosol Forcing in [Wm-2]
Surface Aerosol Forcing in [Wm-2]
Total Water Vapor Content in [gcm-2]

Fig. 12

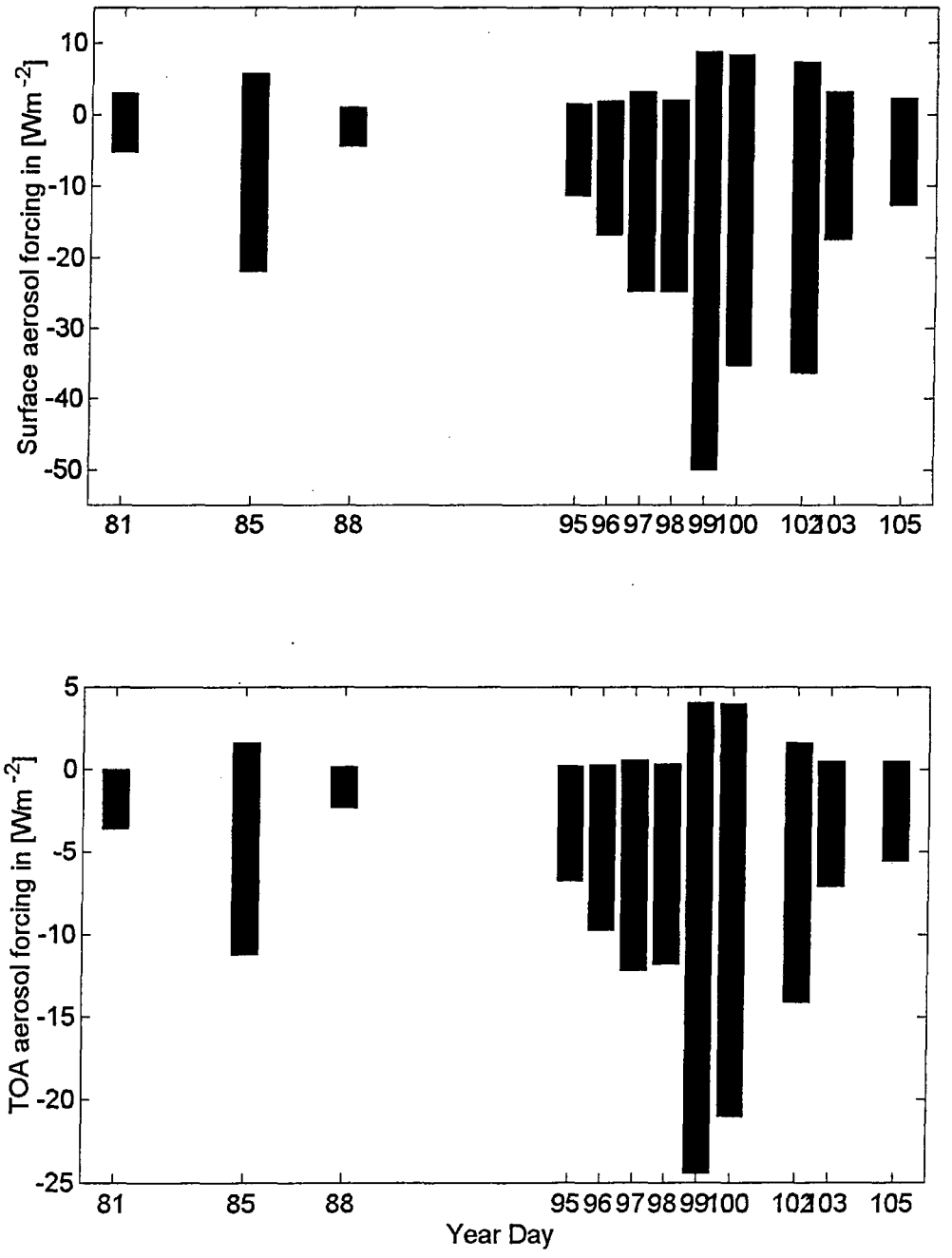
Surface aerosol forcing in [Wm -2]
10
0
-10
-20
-30
-40
-50
81
85
88
95 96 97 98 99 100 102 103 105
TOA aerosol forcing in [Wm -2]
5
0
-5
-10
-15
-20
-25
81
85
88
95 96 97 98 99 100 102 103 105
Year Day

References

Bates, T. S., Huebert, B. J., Gras, J. L., Griffiths, F. B., and Durkee, P. A. (1998). International Global Atmospheric Chemistry (IGAC) project's first aerosol characterization experiment (ACE 1): Overview. *J. Geophys. R.*, **103,** 16297-16318.

Bohren, C. F., and Huffman, D. R. (1983). Absorption and scattering of light by small particles. J. Wiley and Sons, New York.

Chylek, P., Srivastava, V., Pinnick, R. G., and Wang, R. T. (1988). Scattering of electromagnetic waves by composite spherical particles: experiment and effective medium approximations. *App. Opt.*, **27,** 2396-404.

Dufresne, J. L., Gautier, C., Ricchiazzi, P., and Fouquart, Y. (2002). Longwave scattering effects of mineral aerosols. *J. Atmos. Sci.*, **59,** 1959-1966.

Hanel, G., and Zankl, B. (1979). Aerosol size and relative humidity: Water uptake by mixture of salts. *Tellus,* **31,** 478-486.

Hess, M., Koepke, P., and Schult, I. (1998). Optical properties of aerosols and clouds: The software package OPAC., *Bull. Am. Meteorol. Soc.* **79,** 831-844.

Highwood, E. J., M., H. J., Silverstone, M. D., Newman, S. M., and Taylor, J. P. (2002). Ratiative properties and direct effect of Saharan dust measured by the C-130 aircraft during SHADE.2: Terrestrial spectrum. *J. Geophys. R. (in press)*

Hobbs, P. V. (1999). An overview of the University of Washington airborne measurements and results from the Tropospheric Aerosol Radiative Forcing Observational Experiment (TARFOX). *J. Geophys. R.*, **104,** 2233-2238.

Houghton, J. T. (2001). "Climate change 2001 : the scientific basis : contribution of Working Group I to the third assessment report of the Intergovernmental Panel on Climate Change." Cambridge University Press, Cambridge, U.K. ; New York.

Kaufman, Y. J., Hobbs, P. V., Kirchhoff, V., Artaxo, P., Remer, L. A., Holben, B. N., King, M. D., Ward, D. E., Prins, E. M., Longo, K. M., Mattos, L. F., Nobre, C. A., Spinhirne, J. D., Ji, Q., Thompson, A. M., Gleason, J. F., Christopher, S. A., and Tsay, S. C. (1998). Smoke, Clouds, and Radiation - Brazil (SCAR-B) experiment. *J. Geophys. R.*, **103,** 31783-31808.

Loeb, N. G., and Kato, S. (2002). Top-of-atmosphere direct radiative effect of aerosols over the tropical oceans from the Clouds and the Earth's Radiant Energy System (CERES) satellite instrument. *J. Climate,* **15,** 1474-1484.

Lubin, D., Satheesh, S. K., McFarquhar, G., and Heymsfield, A. J. (2002). The longwave radiative forcing of Indian Ocean tropospheric aerosol. *J Geophys. R. (in press).*

Malm, W. C., Sisler, J. F., Huffman, D., Eldred, R. A., and Cahill, T. A. (1994). Spatial and Seasonal Trends in Particle Concentration and Optical Extinction in the United States. *J. Geophys. R.*, **99,** 1347-1370.

Markowicz, K. M., Flatau, P. J., Quinn, P. K., Carrico, C. M., Flatau, M. K., Vogelmann, A. M., and Liu, M. (2003). Influence of relative humidity on aerosol radiative forcing. *submitted to J. Geophys. Res.*, (in press)

Morys, M., Mims, F. M., Hagerup, S., Anderson, S. E., Baker, A., Kia, J., and Walkup, T. (2001). Design, calibration, and performance of MICROTOPS II handheld ozone monitor and Sun photometer. *J. Geophys. R.*, **106,** 14573-14582.

Myhre, G., and Stordal, F. (2001). Global sensitivity experiments of the radiative forcing due to mineral aerosols. *J. Geophys. R.*, **106,** 18193-18204.

Quinn, P. K., Coffman, D. J., Bates, T. S., Miller, T. L., Johnson, J. E., Voss, K., Welton, E. J., and Neususs, C. (2001). Dominant aerosol chemical components and their

contribution to extinction during the Aerosols99 cruise across the Atlantic. *J. Geophys. R.,* **106,** 20783-20809.

Quinn, P. K., Coffman, D. J., Bates, T. S., Miller, T. L., Johnson, J. E., Welton, E. J., Neususs, C., Miller, M., and Sheridan, P. J. (2002) Aerosol Optical Properties during INDOEX 1999: Means, Variability, and Controlling Factors. *J. Geophys. R. (in press).*

Raes, F., Bates, T., McGovern, F., and Van Liedekerke, M. (2000). The 2nd Aerosol Characterization Experiment (ACE-2): general overview and main results. *Tellus,* **52,** 111-125.

Revercomb, H. E., Buijs, H., Howell, H. B., LaPorte, D. D., Smith, W. L., and Sromovsky, L. A. (1988). Radiometric calibration of IR Fourier transform spectrometers: solution to a problem with the High Resolution Interferometer Sounder. *App. Opt.,* **27,** 3210-18.

Rothman, L. S., Rinsland, C. P., Goldman, A., Massie, S. T., Edwards, D. P., Flaud, J. M., Perrin, A., CamyPeyret, C., Dana, V., Mandin, J. Y., Schroeder, J., McCann, A., Gamache, R. R., Wattson, R. B., Yoshino, K., Chance, K. V., Jucks, K. W., Brown, L. R., Nemtchinov, V., and Varanasi, P. (1998). The HITRAN molecular spectroscopic database and HAWKS (HITRAN Atmospheric Workstation): 1996 edition. *J. Quant. Spectrosc. Radiat. Transfer,* **60,** 665-710.

Satheesh, S. K., and Ramanathan, V. (2000). Large differences in tropical aerosol forcing at the top of the atmosphere and Earth's surface. *Nature,* **405,** 60-63.

Sokolik, I. N., Toon, O. B., and Bergstrom, R. W. (1998). Modeling the radiative characteristics of airborne mineral aerosols at infrared wavelengths. *J. Geophys. R.,* **103,** 8813-8826.

Tegen, I., Lacis, A. A., and Fung, I. (1996). The Influence on Climate Forcing of Mineral Aerosols from Disturbed Soils. *Nature,* **380,** 419-422.

Turpin, B. J., and Lim, H. J. (2001). Species contributions to PM2.5 mass concentrations: Revisiting common assumptions for estimating organic mass. *Aerosol Science and Technology* **35,** 602-610.

Vogelmann, A. M., Flatau, P. J., Szczodrak, M., Markowicz, K. M., and Minnett, P. J. (2003). Observations of large greenhouse effects for anthropogenic aerosols. *Geophys. Res. Lett.* (in press).

Welton, E. J., Voss, K. J., Gordon, H. R., Maring, H., Smirnov, A., Holben, B., Schmid, B., Livingston, J. M., Russell, P. B., Durkee, P. A., Formenti, P., and Andreae, M. O. (2000). Ground-based lidar measurements of aerosols during ACE-2: instrument description, results, and comparisons with other ground-based and airborne measurements. *Tellus,* **52,** 636-651.

Wiscombe, W. J., and Grams, G. W. (1976). The backscattered fraction in two-stream approximations. *J. Atmos. Sci.,* **33,** 2440-51.